



## Enhanced dual synergistic mechanism of adsorption and ozone triggering via biochar-derived zero-valent bimetal sites for water purification

Yizhen Cheng<sup>a</sup>, Xiaoyu Zhu<sup>b</sup>, Pengwei Yan<sup>a,\*</sup>, Binyuan Wang<sup>a</sup>, Jing Kang<sup>a</sup>, Jimin Shen<sup>a</sup>, Qiang Tan<sup>a</sup>, Xinwei Zhu<sup>a</sup>, Tianhao She<sup>a</sup>, Jinxiang Zuo<sup>a</sup>, Shengxin Zhao<sup>a</sup>, Zhonglin Chen<sup>a,\*</sup>

<sup>a</sup> State Key Laboratory of Urban Water Resources and Environment, School of Environment, Harbin Institute of Technology, Harbin 150090, China

<sup>b</sup> Guangzhou Urban Planning & Design Survey Research Institute, Guangzhou 510060, China



### ARTICLE INFO

**Keywords:**  
Bimetal-supported biochar  
Catalytic ozonation  
Dual synergistic effect  
Density functional theory  
Toxicity alteration

### ABSTRACT

Novel zero-valent iron (ZVI) and zero-valent zinc (ZVZ) bimetal-supported biochar (ZF@BC) was developed for heterogeneous catalytic ozonation (HCO), which demonstrated the unique dual synergistic adsorption and catalysis-induced effective O<sub>3</sub> triggering and interfacial decontamination. ZF@BC exhibited impressive catalytic and structure stabilities for 2-methyl-4-chlorophenoxyacetic acid (MCPA) degradation during long-lasting HCO, which can resist interference from a complex water quality background. Abundant electron-rich oxygen-containing functional groups and defects on BC contributed to the adsorption of MCPA and O<sub>3</sub>, respectively, while the introduced ZVZ was anticipated to expedite O<sub>3</sub> decomposition by facilitating single-electron transfer reduction of O<sub>2</sub> and establishing a robust connection with ZVI. Continuous efficacy of bimetal in three stages enhanced the efficiency of O<sub>3</sub> utilization and hydroxyl radicals (•OH) yield, thereby safely mitigating the associated toxicity of MCPA after treatment. The development of O<sub>3</sub>/ZF@BC introduced a sustainable, long-term decontamination strategy and provided valuable insights for the advancement of HCO.

### 1. Introduction

To mitigate environmental pollution and recycle organic waste, a variety of biomass is used efficiently by converting it into biochar (BC), which is a biomass-derived material resulting from the partial combustion or pyrolysis of carbon-rich biomass [1,2]. Biomass raw materials mainly come from agricultural and forestry residues, including industrial byproducts, and residual sludge from sewage plants [3–5]. Benefiting from its notable attributes of substantial specific surface area and a higher concentration of oxygen-containing active groups, it is adept at adsorbing and catalyzing the oxidation of heavy metals and organic contaminants found in wastewater [6,7]. Thus, the utilization of BC for water pollutant mitigation has gained prominence in recent years, with a particular focus on harnessing the potential of heterogeneous catalytic ozonation (HCO) technology.

HCO primarily hinges on catalysts to break down ozone (O<sub>3</sub>) into hydroxyl radicals (•OH), which has a high oxidation potential (E<sup>0</sup> = 1.8–2.7 V) and facilitates the rapid deconstruction of waterborne pollutants [8,9]. Compared to homogeneous catalytic ozonation, it has the distinct advantages of non-selectivity, potent oxidation capabilities, and

the absence of secondary pollution [10,11]. However, although the technology of using BC in HCO has been widely reported, the poor stability of BC, low mechanical strength and poor oxidation resistance are still formidable obstacles to its further practical application [12]. Hence, the addition of metal components to BC represents a potential strategy for enhancing its performance in addressing this limitation [13]. It has been reported that BC loaded with manganese oxide (MnO<sub>x</sub>) and iron oxide (FeO<sub>x</sub>) exhibited significantly improved catalytic ozonation capabilities compared to bare BC, accomplishing dechlorination effect improved by 4.1 and 5.3 times compared to pure ozonation [14]. However, a limitation remains evident in real water and carbonate environments, with its poor stability often resulting in the inevitable leaching of metal ions. For these reasons, it is urgent to establish a stable and efficient catalytic ozonation system for practical application.

Bimetallic materials offer not only a greater number of catalytic active sites but also the potential for synergistic interactions between different metals. These synergies can substantially enhance both the catalytic activity and overall stability compared to mono-metallic systems [15]. Furthermore, the nano zero-valent iron (ZVI) has been proven to catalytic ozonation for environmental remediation because of

\* Corresponding authors.

E-mail addresses: [pengweiyuan\\_hit@163.com](mailto:pengweiyuan_hit@163.com) (P. Yan), [zhonglinchen@hit.edu.cn](mailto:zhonglinchen@hit.edu.cn) (Z. Chen).

its low reduction potential ( $E^0_{\text{Fe}^{2+}/\text{Fe}^0} = -0.44\text{V}$ ) [16]. As a trace element in the human body, zinc (Zn) is deemed safe and environmentally friendly. Meanwhile, zero-valent zinc (ZVZ) stands out as a more active reducing agent compared to ZVI, facilitating electron transfer to  $\text{O}_3$  and expediting the HCO process [17]. Moreover, as its oxidized product,  $\text{ZnO}$  has exhibited impressive performance in the realm of catalytic ozonation applications [18]. The potent synergy between these bimetal components has the potential to overcome the prevailing technical challenges mentioned above, ensuring sustained and effective HCO performance.

2-Methyl-4-chlorophenoxyacetic acid (MCPA) serves as a prominent phenoxyacetic acid herbicide, garnering widespread application in agriculture owing to its manifold benefits in enhancing crop yields [19, 20]. However, MCPA does possess certain attributes, including high fluidity, moderate water solubility, low soil adsorption potential, and limited biodegradability [21, 22]. Recognized as a potential threat to human health, MCPA has been designated as a hazardous compound by the World Health Organization (WHO). Furthermore, the International Agency for Research on Cancer (IARC) has also categorized MCPA for specific studies and classified it as a potential human carcinogen [23]. Unfortunately, there is a paucity of research on the removal of MCPA, and the pursuit of scientific and efficient HCO for MCPA removal needs to be paid more attention to.

In this study, a zero-valent bimetallic catalyst was designed, which was incorporated with BC in HCO for MCPA degradation. An interfacial mechanism involving adsorption coordinated with catalysis was unveiled. Comprehensive stability testing was conducted to assess the influence of diverse impurities to gauge the practical application potential. Simultaneously, a comprehensive toxicity assessment of MCPA intermediates for aquatic plants, bacteria, and cellular structures was undertaken, which offered significant insights for the prospective advancement of HCO technology in the future.

## 2. Materials and methods

### 2.1. Materials

Rice straws were gained from a cornfield in Harbin, China. Citric acid (99%), 2-methyl-4-chlorophenoxyacetic acid (MCPA, 99%), *tert*-butanol (TBA, 99%), dimethyl sulfoxide (DMSO, 99.9%), furfuryl alcohol (FFA, 98%), methanol (MeOH, 99%), chloroform (99%) were supplied by Aladdin Biochemical Co., Ltd (China). 5,5-Dimethyl-1-pyrroline N-oxide (DMPO, >97%) and 2,2,6,6-tetramethyl-4-piperidinol (TEMP, >99%) were purchased from Merck Co., Ltd (Germany). Zinc (II) nitrate hexahydrate ( $\text{Zn}(\text{NO}_3)_2 \cdot 6 \text{H}_2\text{O}$ , 99%) and iron (III) nitrate hexahydrate ( $\text{Fe}(\text{NO}_3)_3 \cdot 9 \text{H}_2\text{O}$ , 99%) were obtained from Macklin Biochemical Co., Ltd (China). All experiments were conducted with deionized (DI) water.

### 2.2. Preparation of ZF@BC

The bimetallic zinc-iron-loaded biochar (ZF@BC) was prepared using a one-pot method. 3 g rice straw powder (screened with 40 mesh) was first uniformly dispersed in 50 mL aqueous solution. Then, a certain amount of  $\text{Zn}(\text{NO}_3)_2 \cdot 6 \text{H}_2\text{O}$ ,  $\text{Fe}(\text{NO}_3)_3 \cdot 9 \text{H}_2\text{O}$ , and citric acid were mixed into the solution with the molar ratio of 1:2:3 and evenly stirred for 4 h. After the mixture was dried in an oven at 80 °C for 12 h, the dried solid was ground using a mortar and pestle, and then placed into a tube furnace for calcination at different temperatures (400–900 °C) for 2 h. When the pre-sample was naturally cooled down, it was repeatedly washed with distilled water until the pH of the washing solution became neutral. Finally, it was dried in an oven at 80 °C and stored under dry and cool conditions for future use. The prepared samples were denoted as ZF@BC-Ts ( $T = 400, 500, 600, 700, 800$  and 900). For comparison, the sample without metal, rice straw,  $\text{Fe}(\text{NO}_3)_3 \cdot 9 \text{H}_2\text{O}$  or  $\text{Zn}(\text{NO}_3)_2 \cdot 6 \text{H}_2\text{O}$  were also synthesized, named BC,  $\text{ZnFe}_2\text{O}_4$ , Zn@BC and Fe@BC, respectively. The characterizations of their morphology and

properties were provided in [Text S1](#).

### 2.3. Experimental procedures

The reaction apparatus for HCO is shown in [Fig. S1](#). In a typical experiment, 1 mg/L MCPA solution was dissolved in a 1 L semi-batch glass flask reactor. Then, 70 mg/L catalyst was added into the reaction solution, and  $\text{O}_3$  was continuously injected by an  $\text{O}_3$  generator (COM-AD-01, ANSEROS, Germany) equipped with high-purity oxygen (99.99%). At different intervals (1 min, 3 min, 5 min, 7 min, 10 min and 15 min), 1 mL solution was taken from the system and quenched immediately with  $\text{Na}_2\text{SO}_3$ . Subsequently, the catalysts were filtered with 0.22  $\mu\text{m}$  PTFE filters for further UPLC measurement. To estimate the reusability, the catalyst was collected immediately after each cycle. All experiments were conducted in triplicate to obtain an average value.

### 2.4. Analysis methods

MCPA was determined by ultrahigh-performance liquid chromatography (UPLC, Agilent 1290, USA) equipped with a C18 column. The VWD detector was used and the wavelength was set at 230 nm. The column temperature was set at 30 °C, the injection volume was 100  $\mu\text{L}$ , and the mobile phase was 65% methanol and 35% formic acid water with a flow rate of 0.2 mL/min. The intermediates were investigated by a UPLC-QTOF/MS spectrometer (Agilent 6545, USA). Ion chromatography (ICS-OES, iCAP 7400, Thermo, Germany) was employed to evaluate the leached zinc ions. The concentration of dissolved  $\text{O}_3$  was measured by indigo [24]. The calculation methods of the  $\text{O}_3$  utilization efficiency ( $R_u$ ),  $\text{O}_3$  effective utilization ( $\eta$ ), and the ratio between  $\cdot\text{OH}$  exposure and  $\text{O}_3$  exposure ( $R_{\text{cl}}$ ) are displayed in [Text S2-S4](#).

### 2.5. Theoretical calculations

The adsorption models between MCPA and different configurations of ZF@BC were built by Gaussian 16 software. Then, these models were optimized geometrically according to the B3LYP hybridized function with a 6-311 G basis set and dispersion correction (DFT-D3) [25]. The ZF@BC models with different functional groups were neutral clusters. The natural population analysis (NPA) charge and surface electrostatic potential (ESP) distributions were provided by Gauss View 6.0.16 package according to corresponding optimized models. The adsorption energies ( $E_{\text{ads}}$ ) of different models were calculated by [Eq. \(1\)](#).

$$E_{\text{ads}} = E_{\text{catalyst+MCPA}} - E_{\text{catalyst}} - E_{\text{MCPA}} \quad (1)$$

where  $E_{\text{catalyst+MCPA}}$ ,  $E_{\text{catalyst}}$  and  $E_{\text{MCPA}}$  are the energies of the MCPA adsorbed onto the catalyst, single catalyst, and single MCPA molecule, respectively.

The frontier electron density values ( $\text{FED}_{\text{HOMO}}^2 + \text{FED}_{\text{LUMO}}^2$ ,  $2\text{FED}_{\text{HOMO}}^2$ ) based on frontier electron density theory and bond orders comparison were applied to predict the reaction sites of ATZ and its degradation products by Multiwfn\_3.8\_dev [26]. The higher value of  $\text{FED}_{\text{HOMO}}^2 + \text{FED}_{\text{LUMO}}^2$  or  $2\text{FED}_{\text{HOMO}}^2$  is likely to be attacked by free radicals or electrophilic reactions, respectively. Notably, the highest occupied molecular orbitals (HOMO) and the lowest unoccupied molecular orbitals (LUMO) were calculated by the Gaussian 16 package based on the B3LYP hybridized level and 6-311 G base [27].

### 2.6. Toxicity assessment

The ECOSAR (version 2.2) software was used to predict acute and chronic toxicity. The toxicity assessment of MCPA and its treated solution on pea seedlings was performed by using 70% FAA fixating solution for paraffin sections, and the slides were stained with safranin and fast green to observe the changes in the roots [28].

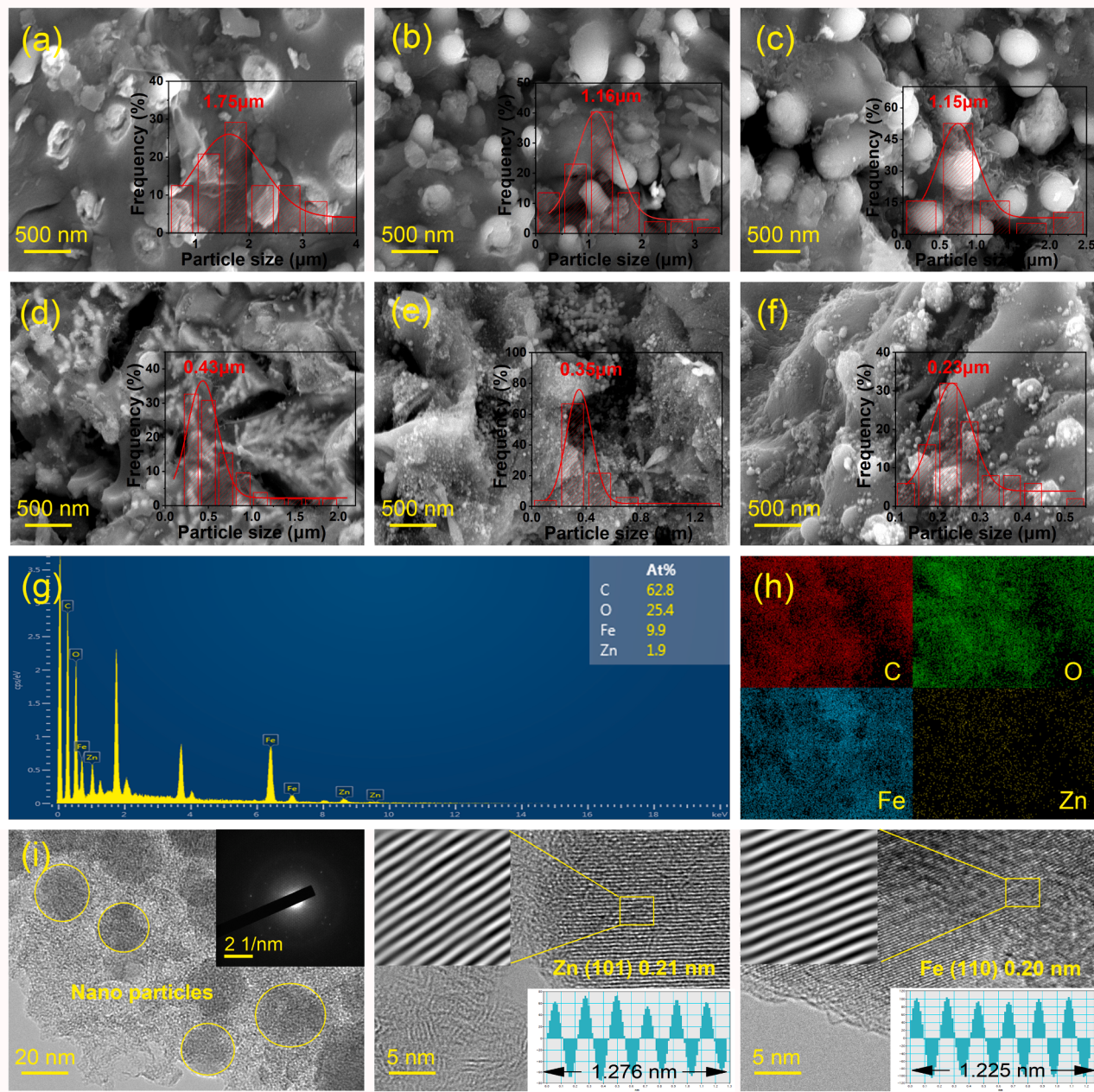


**Fig. 1.** Surface morphology analysis of the catalysts. SEM images and particle size distributions (inset) of (a) ZF@BC-400, (b) ZF@BC-500, (c) ZF@BC-600, (d) ZF@BC-700, (e) ZF@BC-800 and (f) ZF@BC-900. (g) EDS mapping, (h) element distributions and (i) HRTEM images of ZF@BC-800.

### 3. Results and discussion

#### 3.1. Characterization of the Catalysts

##### 3.1.1. Surface morphology

As shown in Fig. 1a-f, the surface morphologies of ZF@BC-Ts were wrinkled and accompanied by nanoparticles (NPs) of different sizes, which were significantly different from the flat and smooth surface of BC (Fig. S1). This may be due to the formation of metal NPs during the calcination process, which disrupted the structure of the BC substrate. In particular, the metal NPs exhibited a variety of particle sizes, with particles gradually decreasing in size and dispersing as the pyrolysis temperature increased. It was attributed to the decomposition of the precursor (citric acid) under high-temperature conditions, which promoted the creation of a loose and porous BC environment, thereby facilitating the formation and deposition of small particles [29]. Fig. 1g

and h shows that ZF@BC-800 was mainly consistent with the elements of C, O, Zn and Fe, which uniformly dispersed on the surface. It is worth noting that the O atoms in ZF@BC-800 may tend to bond with C atoms to create oxygen-containing functional groups rather than Zn and Fe atoms because citric acid readily introduced carboxyl groups onto the BC surface through esterification [30]. This can be further demonstrated in the lattice of HRTEM images displayed in Fig. 1i. Many uniform round dark lines surrounded by disordered graphitic lattice were observed, where two legible lattice stripes (0.21 nm and 0.20 nm) can be identified, corresponding to the (101) planes of ZVZ and the (110) planes of ZVI, respectively [31,32]. These results indicate that ZVZ and ZVI NPs were successfully loaded in the graphitic carbon layer.

##### 3.1.2. Crystal Structure

Due to the coarse surface and high calcium content of BC (Fig. S3), it usually shows low catalytic activity in HCO [33]. Fig. 2a suggests that

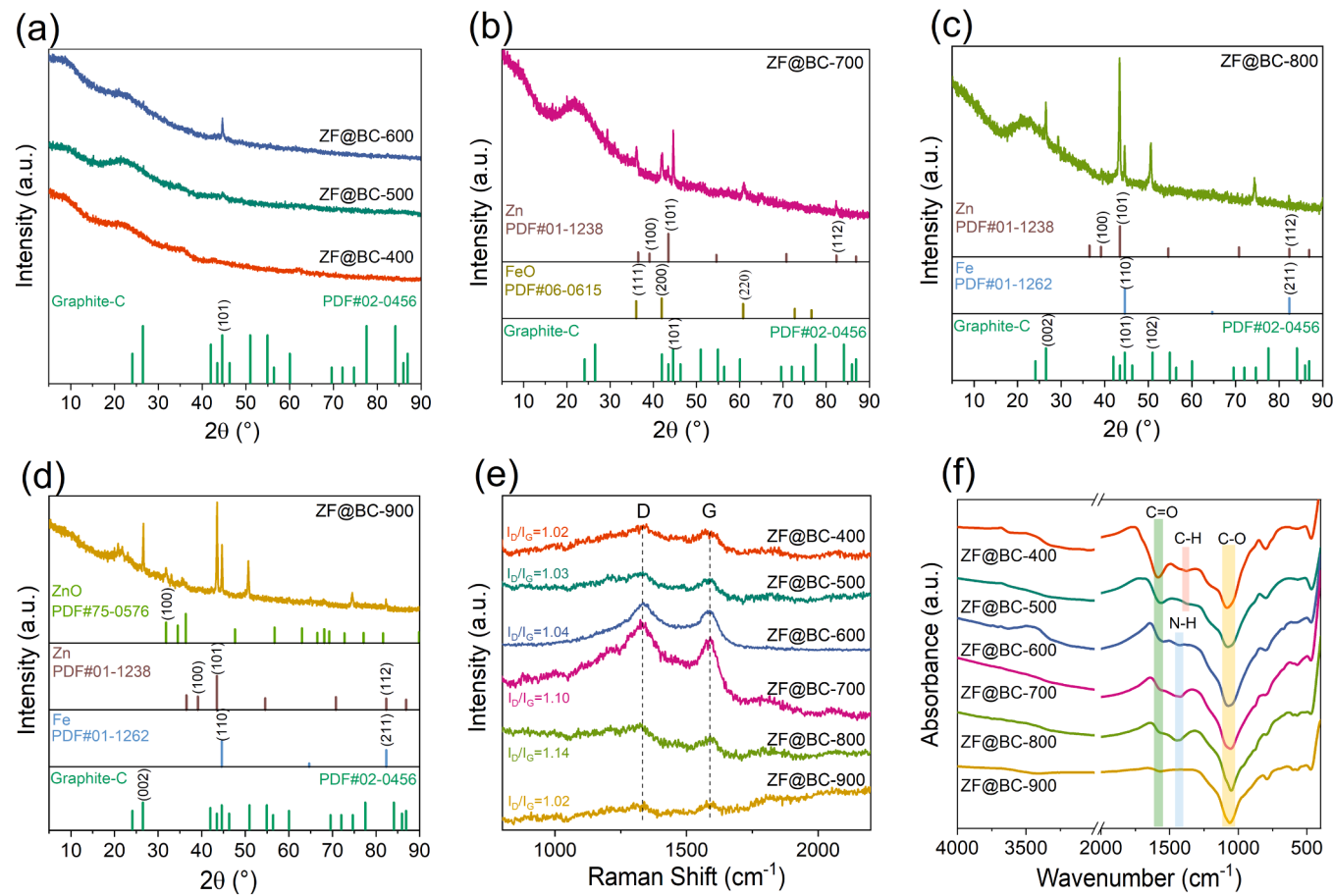


**Fig. 2.** Characterizations of the catalysts. XRD spectra of (a) ZF@BC-400, ZF@BC-500, ZF@BC-600, (b) ZF@BC-700, (c) ZF@BC-800, (d) ZF@BC-900. (e) Raman spectra of ZF@BC-Ts and (f) FT-IR spectra of ZF@BC-Ts.

lower pyrolysis temperature led to poorer crystallinity of ZF@BC-400 and ZF@BC-500 [34]. A characteristic peak of graphitic carbon at  $2\theta = 44.6^\circ$  appeared in ZF@BC-600, indicating that the degree of graphitization of ZF@BC increased with the increase of calcination temperature. Additionally, more crystal faces were identified in ZF@BC-700 except for graphitic carbon, corresponding to ZVZ (PDF#01-1238) and FeO, respectively (Fig. 2b). When the pyrolysis temperature reached 800 °C, a non-oxidizing state of the metal was present in ZF@BC-800, with only the signals of ZVZ and ZVI (PDF#01-1262) being retained (Fig. 2c) [35]. However, Fig. 2d shows that this phenomenon cannot be maintained at higher temperatures (900 °C) because its strength weakened in ZF@BC-900 but a distinct ZnO crystal phase (PDF#75-0576) appeared. Therefore, the pyrolysis temperature has a considerable influence on the form of Zn and Fe components on BC, which varied their HCO performance. Raman spectra can not only reflect the graphitic degree in BC but also show the defect degree through the value of  $I_D/I_G$  [36]. As shown in Fig. 2e, all ZF@BC-Ts had only disordered (D) carbon band ( $1365\text{ cm}^{-1}$ ) and graphitic (G) carbon band ( $1588\text{ cm}^{-1}$ ), showing that BC components are the main body of ZF@BC-Ts. Moreover, ZF@BC-800 achieved a maximum  $I_D/I_G$  value of 1.14, confirming the presence of numerous marginal and structural flaws. Such a high defect level is typically associated with high catalytic activity in HCO [37].

### 3.1.3. Surface area and functional groups

The high specific surface area (SSA) has been recognized as the main characteristic of BC [38]. Fig. S4 demonstrates that with the increase of pyrolysis temperature, the SSA of ZF@BC-Ts increased gradually and reached the maximum of  $194.1\text{ m}^2/\text{g}$  when synthesized at 900 °C. All ZF@BC-Ts exhibited a consistent range of pore size at around

3.7–3.8 nm (Table S1), which effectively provided the required channels for the adsorption and catalytic reaction of MCPA molecules. Furthermore, oxygen-containing functional groups are also recognized as the adsorption and catalytic sites [39]. As shown in Fig. 2f, a stretching of the C=O bond was observed at  $1596\text{ cm}^{-1}$  which gradually weakened as the calcination temperature increased. Similarly, the C-H bending and N-H stretching at  $1440\text{--}1380\text{ cm}^{-1}$  also weakened because high-temperature pyrolysis progressively eliminated the C-H bending and N-H stretching associated with fatty chains [40]. Moreover, a signal at  $1240\text{ cm}^{-1}$  was attributed to C-O vibration, which increased as the pyrolysis temperature increased to 800 °C and then decreased [41]. Thus, the ample SSA and the presence of abundant oxygen-containing functional groups were likely to enhance the mass transfer of organic pollutants or  $\text{O}_3$  thus benefiting interfacial reaction efficiency.

### 3.2. Catalytic performance and stability evaluation

Considering the notable influence of pyrolysis temperature on the physicochemical properties of ZF@BC-Ts, their performances for MCPA degradation during HCO were investigated. As shown in Fig. 3a, the apparent rate constant ( $k_{obs}$ ) of the  $\text{O}_3/\text{ZF@BC-800}$  system was  $0.153\text{ min}^{-1}$  in the 15-minute, which was expressly higher than other catalytic systems, as well as the  $\text{O}_3$  alone ( $0.061\text{ min}^{-1}$ ) and  $\text{O}_3/\text{BC}$  ( $0.065\text{ min}^{-1}$ ) systems (Fig. S5). Therefore, it suggested that the synergy of BC and ZVZ/ZVI components sharply increased the interfacial decontamination efficiency. ZF@BC-800 (simplified as ZF@BC) was employed for the subsequent efficacy and mechanism exploration. As shown in Fig. 3b, ZF@BC exhibited a significant enhancement in MCPA adsorption, achieving a 51.6% removal rate compared to other catalysts,

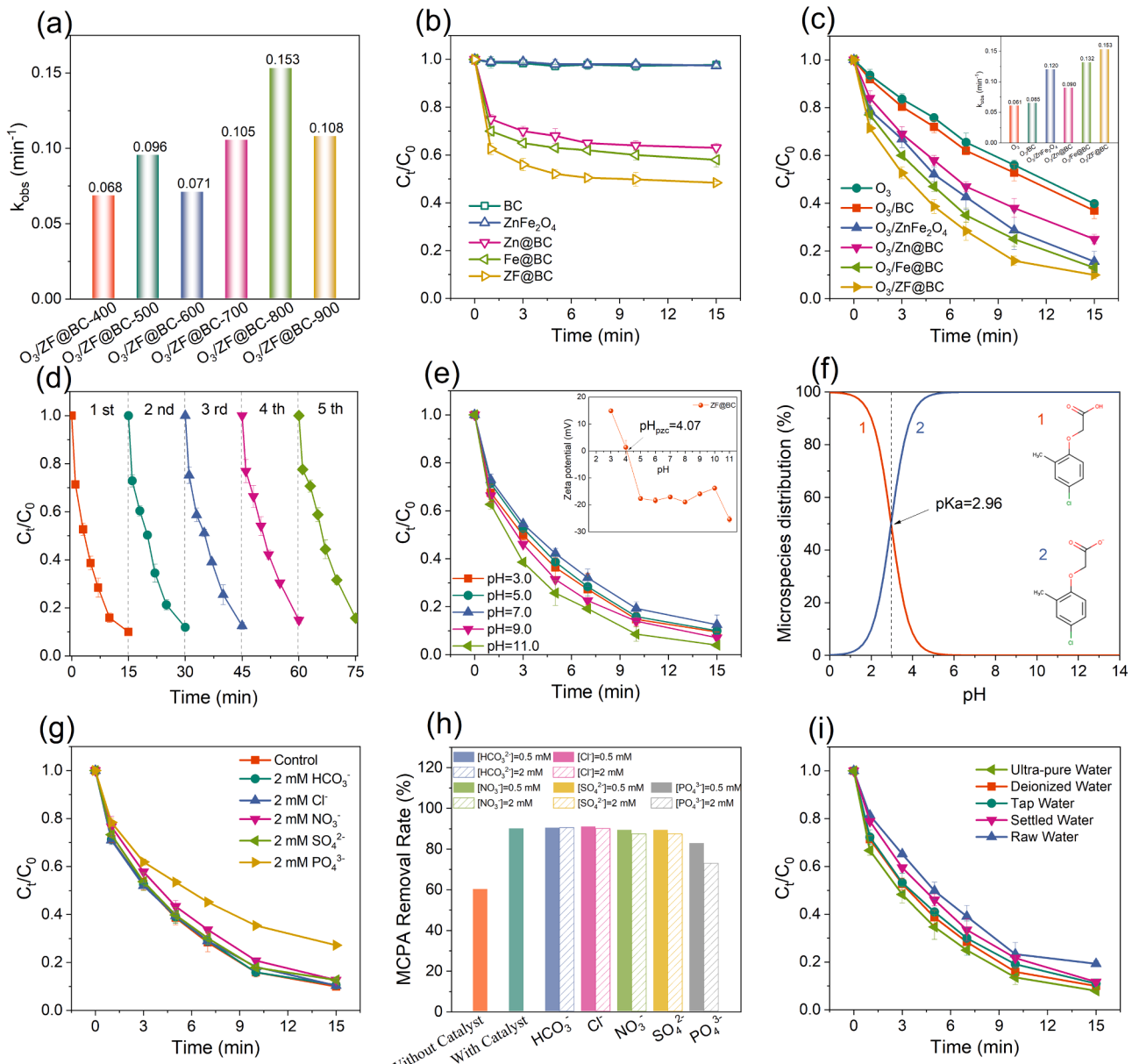


**Fig. 3.** Catalytic activity of the catalysts. (a) The  $k_{obs}$  values MCPA removal in  $O_3/ZF@BC$ -Ts system. (b) Adsorption of MCPA on catalysts. (c) Removal rate of MCPA and corresponding  $k_{obs}$  in different ozonation systems. (d) Reusability tests of ZF@BC. (e) Influence of solution pH for MCPA removal in  $O_3/ZF@BC$  system and  $pH_{pzc}$  of ZF@BC (insert). (f) Microspecies distribution of MCPA at different pH. (g) Influence of anion and (h) corresponding  $k_{obs}$  values for MCPA removal in  $O_3/ZF@BC$  system. (i) Different water backgrounds on MCPA removal in  $O_3/ZF@BC$  system. Conditions:  $[MCPA]_0 = 1.0 \text{ mg/L}$ ,  $[\text{catalyst}] = 70 \text{ mg/L}$ ,  $[O_3] = 10 \text{ mg/L}$ ,  $T = 298 \text{ K}$  and  $\text{pH} = 5.0$ .

which effectively initiated the onset of interfacial catalysis. Predictably, Fig. 3c shows that it did display excellent catalytic ozonation for MCPA removal (90.0%) when contrasted with pure  $ZnFe_2O_4$  (84.4%),  $Zn@BC$  (75.0%), and  $Fe@BC$  (87.0%). The corresponding  $k_{obs}$  value of the  $O_3/ZF@BC$  system registered 1.3, 1.7 and 1.2 folds over these inferior catalytic systems, respectively. Moreover, as the catalyst dosage increased, the removal rate of MCPA exhibited a gradual increase (Fig. S6a). However, the degradation rate of high-concentration MCPA was diminished, attributed to the depletion of the ROS by various intermediate products (Fig. S6b). As a result, the exceptional MCPA removal efficiency resulted from the well-behaved solid-liquid interface reaction.

Given the impressive catalytic performance of ZF@BC, an examination of its catalytic stability was also conducted. As shown in Fig. S7, ZF@BC has almost no metal ( $Zn^{2+}$  and  $Fe^{2+}$ ) leaching during HCO compared to  $ZnFe_2O_4$ . It may be benefited from its relatively low loading

of  $Zn$  (3.1 wt%) and  $Fe$  (7.7 wt%) in ZF@BC compared with  $ZnFe_2O_4$  (Table S2). Meanwhile, it still maintained more than 85% MCPA removal rate after 5 consecutive uses, exhibiting excellent recycling stability (Fig. 3d). Considering the complexity of actual water bodies, it is imperative to investigate the stability of  $O_3/ZF@BC$  in overcoming the interference arising from diverse water quality backgrounds. From Fig. 3e, overall, the removal of MCPA obtained a satisfactory effect in the  $O_3/ZF@BC$  system under varied solution pH. It seems that the acidic environment was more conducive to MCPA degradation when the pH was less than 7.0, making the removal effect at  $\text{pH} = 3.0$  (90.5%) better than that at  $\text{pH} = 5.0$  (90.0%) and  $\text{pH} = 7.0$  (87.5%). This phenomenon arose from the fact that the  $pH_{pzc}$  of ZF@BC is 4.07 and the surface of ZF@BC predominantly carried a positive charge when the solution pH was 3.0. Simultaneously, MCPA primarily existed in a dissociation form with a  $pK_a$  of 2.96 (Fig. 3f), such kind of electrostatic attraction

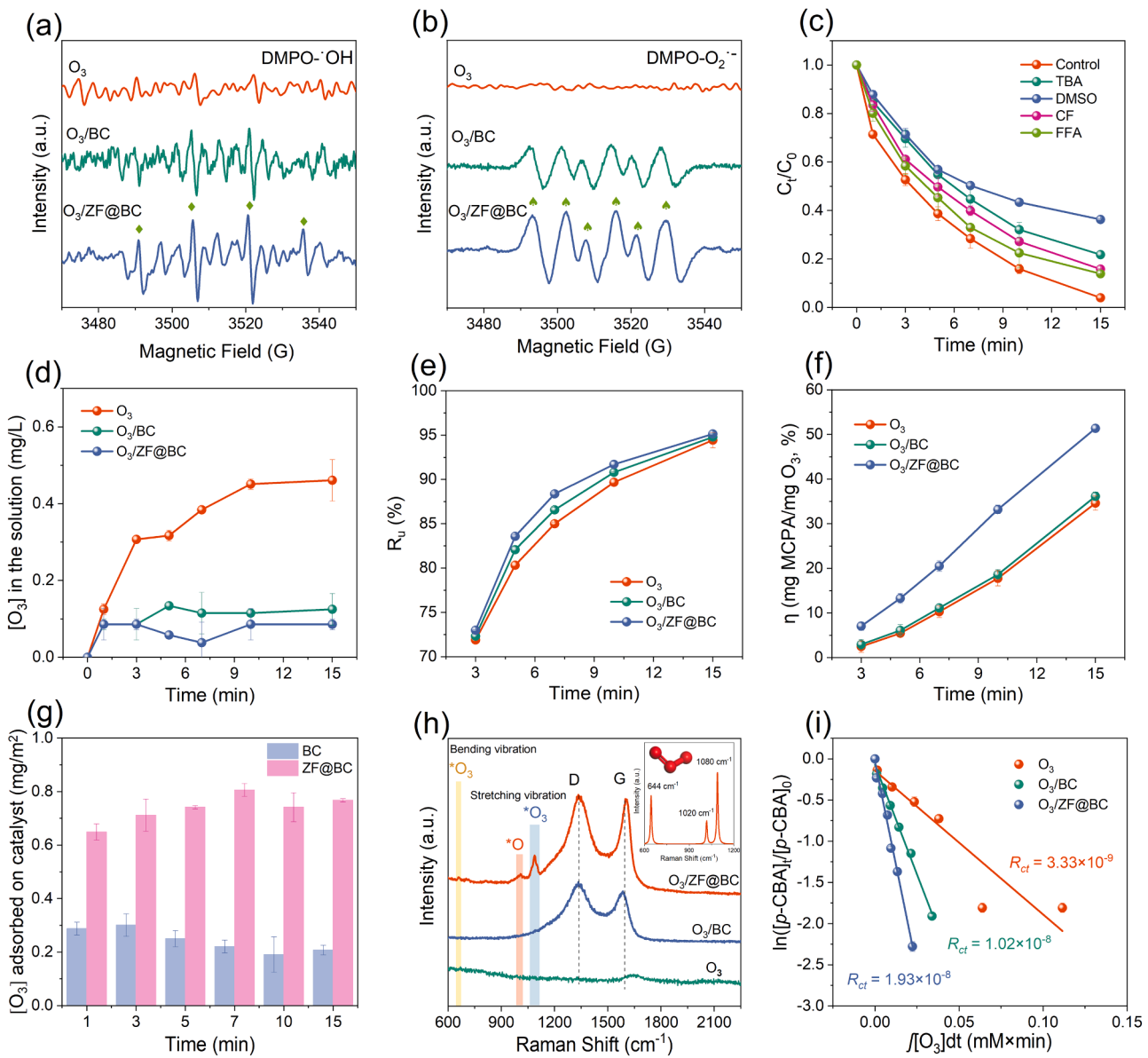
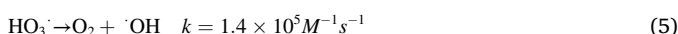
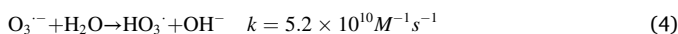
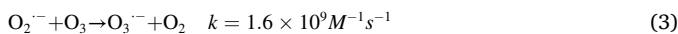
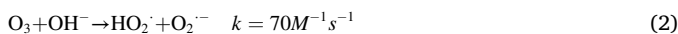


**Fig. 4.** Investigation of ROS. ESR identification of (a) hydroxyl radicals and (b) superoxide radicals. (c) Effects of ROS scavengers on MCPA removal. (d) The concentration of O<sub>3</sub> in the solution. (e) O<sub>3</sub> utilization efficiency ( $R_u$ ) and (f) O<sub>3</sub> effective utilization ( $\eta$ ) in different ozonation systems. (g) The concentration of O<sub>3</sub> adsorbed on the catalyst. (h) In-situ Raman spectra in different ozonation systems. (i) Calculation of  $R_{ct}$  values in different ozonation systems. Conditions: [MCPA]<sub>0</sub> = [p-CBA]<sub>0</sub> = 1.0 mg/L, [catalyst] = 70 mg/L, [O<sub>3</sub>] = 10 mg/L, T = 298 K and pH = 5.0.

facilitated the interface catalytic process [42]. Nonetheless, as the pH value gradually rose to 5.0 and 7.0, the surface of ZF@BC became predominantly negatively charged. Consequently, the electrostatic repulsion between MCPA and ZF@BC hindered the accessibility of certain catalytic sites [43]. The enhancement of the MCPA removal in an alkaline environment (pH > 7.0) may be attributed to the contribution of the hydroxide (OH<sup>-</sup>) (Eqs. (2–5)), making homogeneous catalysis dominant at this moment rather than heterogeneous catalysis.



Addressing anion (HCO<sub>3</sub><sup>-</sup>, Cl<sup>-</sup>, NO<sub>3</sub><sup>-</sup>, SO<sub>4</sub><sup>2-</sup>, PO<sub>4</sub><sup>3-</sup>) interference in real

water presents another significant challenge to overcome in practical applications [44]. As shown in Fig. 3g, only a 17.2% decrease in MCPA degradation by 2.0 mM PO<sub>4</sub><sup>3-</sup>, which would act as a stronger Lewis base compared to a water molecule (H<sub>2</sub>O) to reduce MCPA degradation by replacing the hydrated hydroxyl group (–OH) formed on metal sites [45]. Surprisingly, HCO<sub>3</sub><sup>-</sup> did not noticeably affect the degradation of MCPA, although it usually acts as an inhibitor of <sup>•</sup>OH ( $k_{OH/HCO_3^-} = 3.9 \times 10^8 M^{-1} s^{-1}$ ) [12]. This may be due to the negative charge on the ZF@BC surface under neutral conditions, and the electrostatic repulsion reduced HCO<sub>3</sub><sup>-</sup> interference. The same anti-interference phenomenon was also observed in the experiments where Cl<sup>-</sup>, NO<sub>3</sub><sup>-</sup> and SO<sub>4</sub><sup>2-</sup> existed. Natural organic matter (NOM) is ubiquitously found in actual water bodies, potentially occupying adsorption sites of carbon-based catalysts and impeding the degradation of contaminants [46]. Interestingly, even with a high concentration of NOM (5 mgC/L), MCPA consistently achieved ~80% removal rate (Fig. S8). It underscores that the combined adsorption-oxidation technology exhibit greater stability in resisting

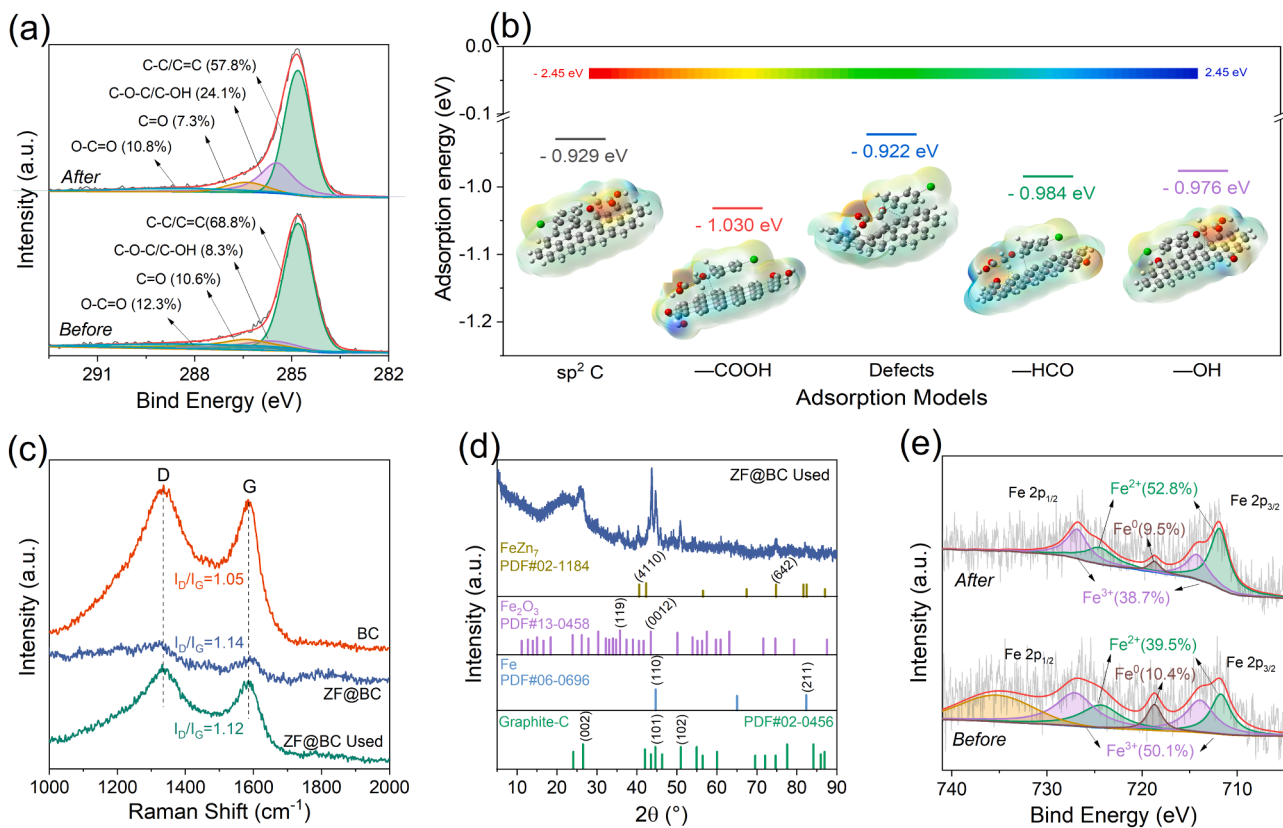


**Fig. 5.** (a) High deconvolution of C 1 s spectra of ZF@BC before and after the reaction. (b) The adsorption energy of MCPA on different adsorption models. (c) Raman spectra of BC and ZF@BC before and after the reaction. (d) XRD spectra of ZF@BC after the reaction. (e) High deconvolution of Fe 2p spectra of ZF@BC before and after the reaction.

interference from diverse water quality factors compared with conventional adsorption technologies. Building upon this, the catalytic efficacy of the O<sub>3</sub>/ZF@BC system was subsequently examined in five distinct water qualities. Fig. 3f shows that although MCPA degradation efficiency sequentially improved as water purity levels increased, the inhibitory effect of raw water on the MCPA removal rate was relatively minimal. It indicates that ZF@BC can induce the reaction of O<sub>3</sub> and MCPA at the interface, which was therefore unaffected by the complex component in the aqueous solution. Hence, in contrast to the conventional HCO, the O<sub>3</sub>/ZF@BC system effectively resisted the interference of the water matrices, and the exceptional catalytic stability of ZF@BC held great practical significance and promising application prospects.

### 3.3. Identification of ROS

The O<sub>3</sub>/ZF@BC system showed high performance compared to the O<sub>3</sub> @BC system, it was believed that the loaded ZVZ and ZVI greatly promoted O<sub>3</sub> decomposition for ROS generation, thus benefitting MACP degradation. ESR spectroscopy was first conducted to identify possible ROS in ZF@BC-induced HCO [47]. As shown in Fig. 4a, the presence of DMPO-•OH adducts was discernible in the O<sub>3</sub> alone, O<sub>3</sub>/BC, and O<sub>3</sub>/ZF@BC systems. Inferring the generation of •OH in all reaction systems, and the highest intensity of the signal by ZF@BC suggested the enhancement in •OH yield. Similarly, the DMPO-O<sub>2</sub><sup>•</sup> signals in the three systems also have the same tendency (Fig. 4b). Demonstrating the highest catalytic efficiency of ZF@BC may be related to the production of high concentration •OH and superoxide radical (O<sub>2</sub><sup>•</sup>). Subsequently, quenching experiments were further used to verify this conjecture.

Based on the fast reaction between TBA ( $k_{\text{OH/TBA}} = 6.0 \times 10^8 \text{ M}^{-1} \text{s}^{-1}$ ) and DMSO ( $k_{\text{OH/DMSO}} = 5.4 \times 10^9 \text{ M}^{-1} \text{s}^{-1}$ ) with •OH, TBA and DMSO were used to quench •OH in the O<sub>3</sub>/ZF@BC system [48].

Likewise, CF is an ideal quenching agent for O<sub>2</sub><sup>•</sup> because of its faster reaction rate with O<sub>2</sub><sup>•</sup> ( $k_{\text{O}_2^{\bullet-}/\text{CF}} = 2.3 \times 10^8 \text{ M}^{-1} \text{s}^{-1}$ ) but slowly with •OH ( $k_{\text{OH/CF}} = 5.4 \times 10^7 \text{ M}^{-1} \text{s}^{-1}$ ) and O<sub>3</sub> ( $k_{\text{O}_3/\text{CF}} \leq 0.1 \text{ M}^{-1} \text{s}^{-1}$ ) [49]. As shown in Fig. 4c, DMSO has the highest inhibition effect for MCPA degradation, followed by TBA, then CF and FFA. Illustrating the surface •OH (•OH<sub>ad</sub>) on ZF@BC contributed more than •OH in solution because DMSO is more accessible to the catalyst than TBA [50]. Nevertheless, the relatively mild inhibitory impact of DMSO suggests that the robust adsorption of ZF@BC significantly mitigated the assault of inhibitor on the surface ROS. Additionally, the addition of CF and FFA had small inhibitions on the degradation of MCPA, which was probably caused by steric hindrance. As a result, the strengthened interfacial reaction of surface •OH<sub>ad</sub> towards adsorbed MCPA efficiently ensured the decontamination and weakened the interference of various water matrices.

### 3.4. Enhancing interfacial mass transfer of O<sub>3</sub> and MCPA

To explore the interfacial mass transfer of O<sub>3</sub> from water to the ZF@BC surface, the concentration of O<sub>3</sub> in the solution was first monitored. As shown in Fig. 4d, the concentration of O<sub>3</sub> during HCO (0.09 mg/L) was drastically lower than that of the O<sub>3</sub> alone system (0.46 mg/L) in 15 mins. Accordingly, the higher O<sub>3</sub> utilization efficiency ( $R_u = 95.1\%$ ) (Fig. 4e) was found in O<sub>3</sub>/ZF@BC than in other ozonation systems, along with enhanced O<sub>3</sub> effective utilization ( $\eta = 52.7\%$ ) (Fig. 4f). Additionally, ZF@BC exhibited excellent ability to adsorb O<sub>3</sub> (Fig. 4g). Specifically, O<sub>3</sub> was rapidly adsorbed on ZF@BC in the first 1 min and gradually rose to 0.81 mg/m<sup>2</sup> at 7 min, which was 2.6 fold than that of BC. It implies that ZF@BC not only facilitated the mass transfer efficiency of O<sub>3</sub> from bulk water to catalytic surface but also enhanced the efficient adsorption of dissolved O<sub>3</sub> in the interface to actively participate in the degradation of MCPA.

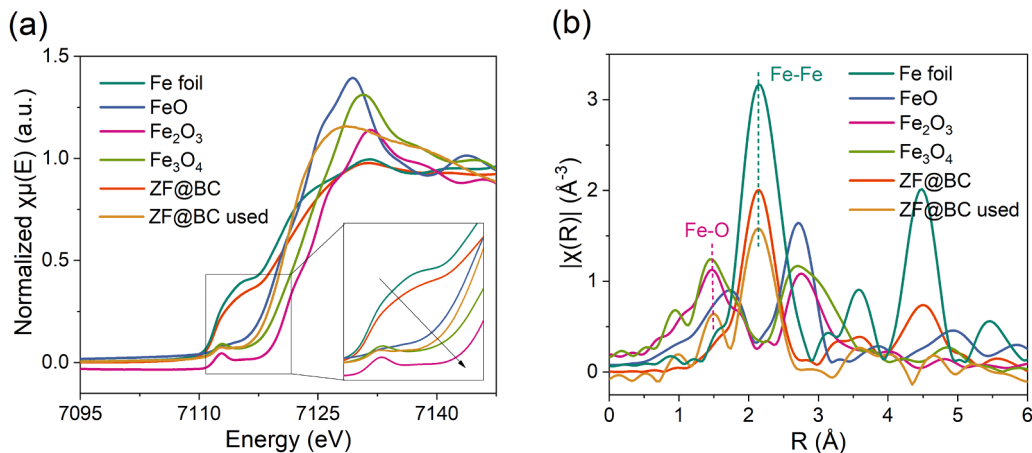


Fig. 6. (a) Normalized Fe K-edge XANES spectra and (b) FT-EXAFS spectra of Fe foil, FeO, Fe<sub>2</sub>O<sub>3</sub>, Fe<sub>3</sub>O<sub>4</sub> and ZF@BC.

More evidently, in-situ Raman technology was further applied to determine the above speculation. However, there was no obvious signal in the O<sub>3</sub> solution, which may be due to the difficulty of signal capture caused by the fluidity of O<sub>3</sub> aqueous solutions. To distinguish the behavior of the adsorbed O<sub>3</sub> on ZF@BC, the standard Raman spectrum of O<sub>3</sub> in aqueous medium was simulated by the Gaussian program (illustration in Fig. 4h). The two strong peaks at 1080 cm<sup>-1</sup> and 644 cm<sup>-1</sup> were attributed to the stretching and bending vibrations of the prolonged O-O bond of O<sub>3</sub>, respectively. The other peak at 1020 cm<sup>-1</sup> was derived from the surface atom oxygen (\*O) species formed by the fracture of O-O stretching. Accordingly, the three signals were also detected in the O<sub>3</sub>/ZF@BC system, especially the stretching vibration of O<sub>3</sub> at 1080 cm<sup>-1</sup> [51]. Thus, it proves that a large amount of O<sub>3</sub> was enriched on the surface of ZF@BC, and partially decomposed to the active \*O on metal sites and the subsequent generation of \*OH.  $R_{ct}$  usually refers to the ratio between \*OH exposure and O<sub>3</sub> exposure. As shown in Fig. 4i, the highest value of  $R_{ct}$  ( $1.93 \times 10^{-8}$ ) in the O<sub>3</sub>/ZF@BC system proved that such synergistic effects between adsorbed and catalyzed O<sub>3</sub> accelerated the conversion of O<sub>3</sub> to \*OH, which further contributed to MCPA degradation [33].

The high removal rate of MCPA on ZF@BC suggested the efficient mass transfer of it on the catalytic surface, thus the behavior of MCPA at the interface is also noteworthy. As shown in Fig. 5a, the carboxyl group (−COOH) and carbonyl group (C=O) may both be involved in MCPA removal, which decreased from 12.3% to 10.8% and 16.6% to 7.3%, respectively. On the one hand, the electron-rich −COOH and C=O would provide electrons for the adsorption and decomposition of O<sub>3</sub> and further be oxidized to other oxygen-containing functional groups (C-O-C or C-OH) [52]. On the other hand, these oxygen-containing functional groups within ZF@BC can also serve a crucial role in facilitating access to MCPA. Fig. 5b reveals the  $E_{ads}$  of MCPA molecules on different functional groups through DFT calculation. Compared with the sp<sup>2</sup> C configuration and defect configuration, the adsorption energies of MCPA by oxygen-containing functional groups were relatively lower, especially the electron-rich −COOH with the lowest  $E_{ads}$  of  $-1.030$  eV. Moreover, our previous work has reported that the defects of BC can effectively adsorb O<sub>3</sub> which was consistent with the decline in  $I_D/I_G$  values after the reaction displayed in Fig. 5c [53]. Thus, the oxygen-containing functional groups and defects within ZF@BC promoted the maximum adsorption of MCPA and O<sub>3</sub> on the catalyst surface, effectively activating the following interface catalytic reaction at the bimetallic site, and avoiding the interference of impurities in water to the greatest extent.

### 3.5. Triggering of the adsorbed O<sub>3</sub> via bimetallic sites

It has been reported that zero-valent metals can decompose O<sub>3</sub>, while metal oxides can promote the formation of hydroxyl groups on the surface, both active sites can thereby increase the yield of ROS [32,54]. Unlike the only remaining ZVI and ZVZ components in fresh ZF@BC, Fig. 5d reveals the presence of two distinctive peaks corresponding to Fe<sub>2</sub>O<sub>3</sub> with low crystallinity and FeZn<sub>7</sub> in ZF@BC following catalytic ozonation, indicating that the original ZVI and ZVZ participated in the reaction and were partially oxidized and form compounds with bared Zn. It suggests that the triggering of O<sub>3</sub> on the catalyst-water interface may go through different processes [55].

In this first stage, ZVI could not only directly strip O<sub>3</sub> to generate \*O and \*O<sub>2</sub> confirmed by in-situ Raman spectra (Eqs. (6–8)), but also as a powerful electron donor ( $E^0_{Fe^{2+}/Fe^0} = -0.44$  V) and react with adsorbed O<sub>3</sub> through the valence cycle (Eq. (9)) [33,56]. This process was consistent with the change in Fe 2p spectra of ZF@BC before and after the reaction (Fig. 5e). To further explore the electronic structure and coordination environments of Fe during catalytic ozonation, the X-ray absorption near edge structure (XANES) and the extended X-ray absorption fine structure (EXAFS) were further performed. As shown in Fig. 6a, XANES analysis of Fe K-edge spectra illustrates an augmented electropositivity of Fe after its interaction with O<sub>3</sub>. In contrast to the initial zero valence of Fe in ZF@BC, a pronounced escalation from zero to +2  $\sim$  +3 was observed after the reaction. From the Fourier-transformed (FT)  $k^3$ -weighted EXAFS spectra (Fig. 6b), ZF@BC displays one main peak at  $\sim 2.21$  Å for Fe-Fe coordination [57]. After reacting with O<sub>3</sub>, another peak at  $\sim 1.50$  Å appeared, signifying the presence of Fe-O bonds. This observation suggests the active participation of ZVI in catalytic ozonation, subsequently undergoing oxidation to form iron oxide. Meantime, ZVZ can enhance O<sub>2</sub><sup>•-</sup> and H<sub>2</sub>O<sub>2</sub> formation through single electron transfer reduction of O<sub>2</sub>, which further accelerated O<sub>3</sub> decomposition and \*OH production by the following chain reaction (Eqs. (10–13)) [18,58]. After the reaction, the hysteresis ring closure of ZF@BC in N<sub>2</sub> adsorption-desorption isotherms was later than the fresh one, indicating that the metal agglomeration may occur in the material after use, increasing the number of holes (Fig. S9).

In the second stage, the triggering of O<sub>3</sub> on ZVZ and ZVI sites caused more Fe<sup>2+</sup> and Zn<sup>2+</sup> exposed on the ZF@BC surface, which contributed to the adsorption and dissociation of water molecules and induced the decomposition of adsorbed O<sub>3</sub> to form \*OH [8,59]. In the third stage, Fe<sup>2+</sup> on ZF@BC can persist in interacting with O<sub>3</sub> and give rise to the production of Fe<sup>3+</sup> (Eq. (14)), which is predisposed to engage with water molecules compared to Fe<sup>2+</sup> and Fe<sup>0</sup> [60]. Consequently, the hydrophilicity of ZF@BC increased significantly after use (Fig. S10), making a large amount of water molecules accumulate on the ZF@BC surface

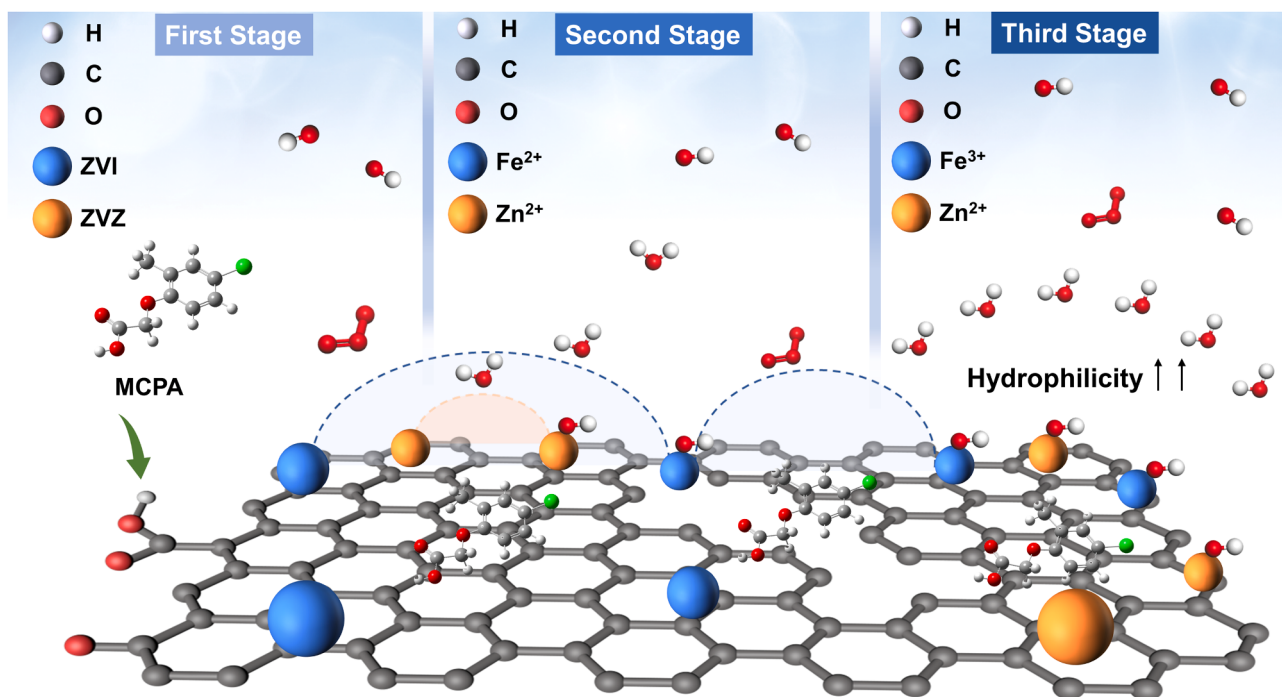


Fig. 7. The sustained trilogy process of ZF@BC in catalytic ozonation.

during this stage, which serves to enhance the ongoing catalysis of  $O_3$  through the dissociation of water molecules on adjacent  $Zn^{2+}$ . This sustained trilogy process effectively ensures the prolonged performance of HCO. (Fig. 7).

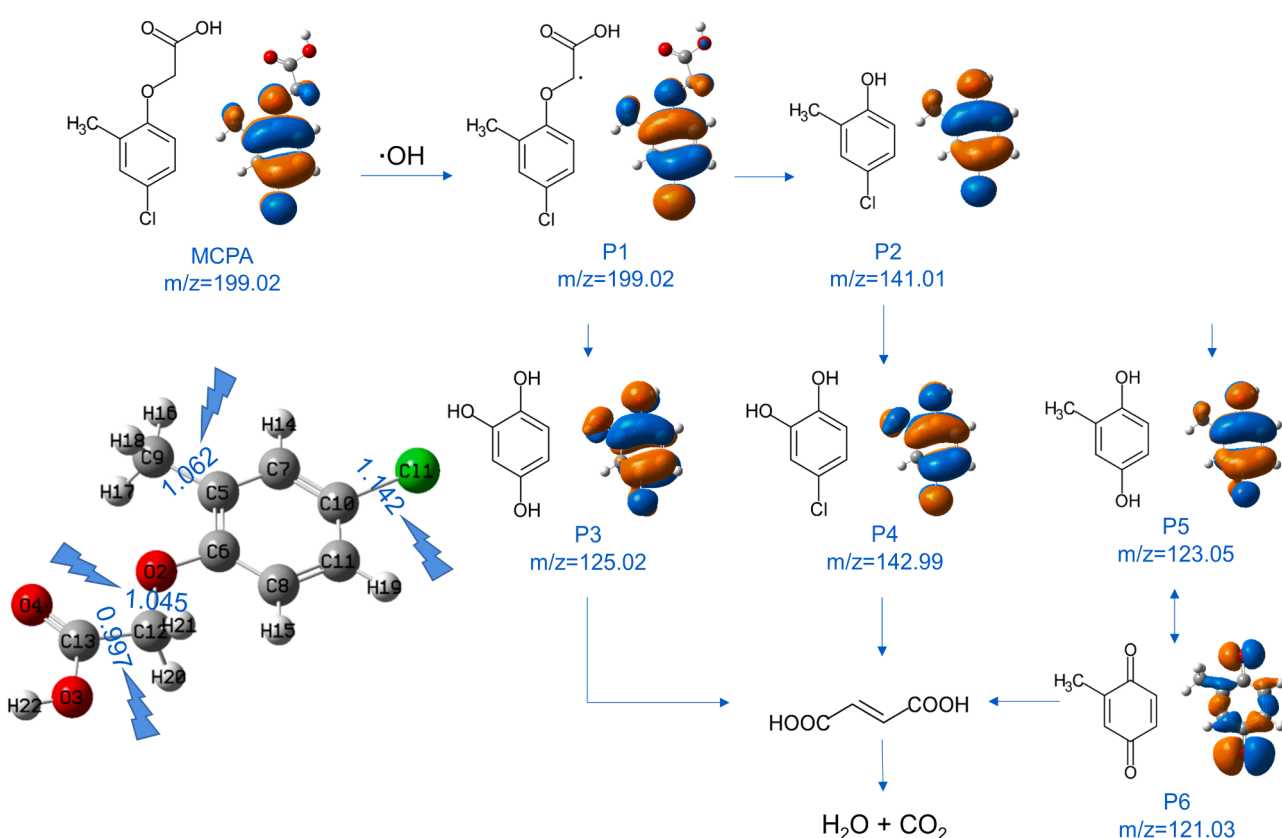
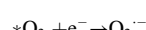
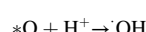
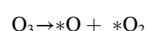
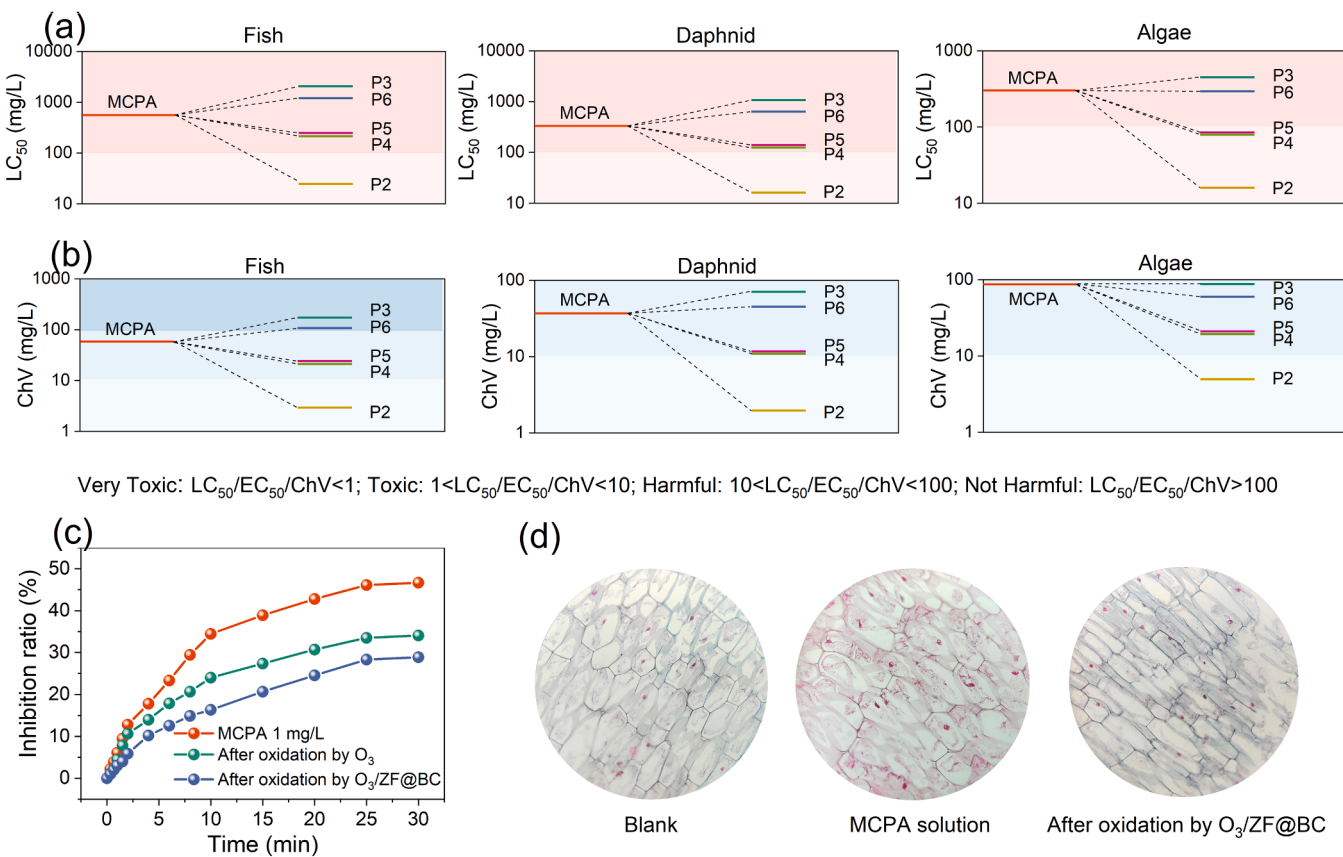
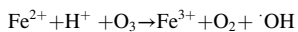
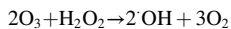
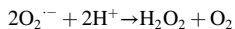
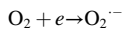
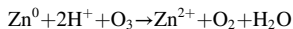
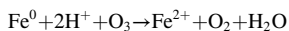


Fig. 8. Possible degradation pathway of MCPA in the catalytic ozonation system.



**Fig. 9.** (a) Acute toxicity and (b) chronic toxicity of MCPA and its intermediate products predicted by ECOSAR. (c) Inhibition ratio of luminous bacteria by different treated solutions. (d) Effect of the solution of MCPA and after oxidation treatment on the cell wall of pea bud.



### 3.6. Deconstruction of MCPA

UPLC-QTOF/MS analysis and DFT calculation were combined to declare the deconstruction products of MCPA during the  $\cdot OH$  attack. The values of the Wiberg bond order were calculated in Table S3, it shows four bonds with small values that may be broken by  $\cdot OH$  attacks, corresponding to 1(Cl)– 10(C), 2(O)– 12(C), 5(C)– 9(C) and 12(C)– 13(C). Regarding the Frontier electron densities (FEDs) theory calculation of MCPA (Table S4), The 2(O) in the ether bond had the highest  $2FED_{HOMO}^2$  value of 0.274415, followed by the 10(C) atom of 0.203197. The higher  $2FED_{HOMO}^2$  value indicates that these two sites had stronger electron-providing capacities, which were more easily oxidized by  $\cdot OH$ . As a result, alkyl-hydroxylation was easy to occur at 2(O) while dechlorinated hydroxylation may appear at 10(C) [61]. Based on theoretical derivation, the total ion chromatogram (Fig. S11) and mass spectrogram (Fig. S12) of MCPA and its intermediate substances produced by the  $O_3/ZF@BC$  system were identified by UPLC-QTOF/MS (Table S5). Finally, a possible degradation pathway of MCPA was proposed in Fig. 8.

At the outset, MCPA underwent an initial reaction with  $\cdot OH$ , leading

to the dehydrogenation of MCPA to yield P1 and  $H_2O$ . Previous studies have indicated that the hydrogen atom attached to the aromatic ring is less susceptible to extraction by  $\cdot OH$  [62]. Therefore, a hydrogen atom would be extracted from the side chain by  $\cdot OH$ . Then, the side chain P1 will encounter further alkyl-hydroxylation, resulting in the production of P2. As further oxidation, P3, P4, and P5 are generated through dechlorination and electrophilic addition of  $\cdot OH$  [63]. After that, they will continue to be oxidized and ring-opened to form small acid molecules until finally mineralized into  $H_2O$  and  $CO_2$  [64].

### 3.7. Toxicity alteration of the intermediate products

To assess the potential toxicity alteration of MCPA degradation after  $ZF@BC$ -induced HCO. Ecosar was employed to investigate the acute and chronic toxicity of MCPA degradation products on fish, daphnia and green algae. As illustrated in Fig. 9a and b, it was evident that only the P2 products exhibit significant chronic toxicity, whereas the other products demonstrate a relatively low level. This observation confirmed the presence of certain potentially harmful substances in the MCPA degradation process, but it was important to note that these substances were hypotoxic and could be effectively mineralized and eliminated by the  $O_3/ZF@BC$  system. For luminescent bacteria, the inhibition rate of the remaining solution on luminescent bacteria decreased significantly after 30 min treatments under the  $O_3/ZF@BC$  system (Fig. 9c). Additionally, pea seedlings were selected to investigate the effects of MCPA and the treated solution on plant cells. As shown in Fig. 9d, in the blank group, the cell membrane was in close contact with the cell wall, the nucleolus was obvious and the cavity was large. However, high concentrations of MCPA caused damage to the cell wall and vacuole to rupture, which was not observed in the solution treated by the  $O_3/ZF@BC$  catalytic ozonation

technology represents a secure and highly efficient treatment method, holding substantial practical significance.

#### 4. Conclusions

Herein, a ZVI and ZVZ bimetal-supported biochar (ZF@BC) was synthesized. The MCPA degradation efficiency of the O<sub>3</sub>/ZF@BC system reached an impressive level (90.0%), surpassing the performance of O<sub>3</sub> alone, O<sub>3</sub>/BC, O<sub>3</sub>/Zn@BC and O<sub>3</sub>/Fe@BC systems. Notably, minimal metal leaching was observed and the degradation rate of MCPA was only 12.8% decreased even after five repeated uses. The interface mechanism unveiled the synergistic effect of adsorption and catalysis. Abundant electron-rich oxygen-containing functional groups and carbon defects functioned as adsorption sites for MCPA and O<sub>3</sub>, respectively. The bimetallic ZVI and ZVZ components facilitated the decomposition of the adsorbed O<sub>3</sub>. Importantly, the strong interface connection remained unaffected by other impurities in the solution, making this technology highly practical and valuable. Toxicity evaluation results indicate that ZF@BC is an environmentally friendly and safe material, offering a practical approach for the preparation of bimetallic catalysts for ozonation processes.

#### CRediT authorship contribution statement

**Yizhen Cheng:** Writing – original draft, Visualization, Validation, Methodology, Investigation, Conceptualization. **Xiaoyu Zhu:** Data curation. **Pengwei Yan:** Writing – review & editing, Investigation. **Binyuan Wang:** Formal analysis. **Jing Kang:** Formal analysis. **Jimin Shen:** Conceptualization. **Qiang Tan:** Formal analysis. **Xinwei Zhu:** Validation. **Tianhao She:** Validation. **Jinxiang Zuo:** Validation. **Shengxin Zhao:** Formal analysis. **Zhonglin Chen:** Resources, Project administration.

#### Declaration of Competing Interest

The authors declare that they have no known competing financial interests or personal relationships that could have appeared to influence the work reported in this paper.

#### Data Availability

Data will be made available on request.

#### Acknowledgments

The work was funded by National Key Research and Development Program of China (Grant No. 2022YFC3203701-03), Heilongjiang Touyan Innovation Team Program (Grant No. HIT-SE-01), and State Key Laboratory of Urban Water Resource and Environment (Harbin Institute of Technology) (Grant No. 2022TS04, QA202321).

#### Appendix A. Supporting information

Supplementary data associated with this article can be found in the online version at [doi:10.1016/j.apcatb.2023.123618](https://doi.org/10.1016/j.apcatb.2023.123618).

#### References

- [1] C. Liu, L. Chen, D. Ding, T. Cai, From rice straw to magnetically recoverable nitrogen doped biochar: Efficient activation of peroxymonosulfate for the degradation of metolachlor, *Appl. Catal. B: Environ.* 254 (2019) 312–320.
- [2] Y. Chen, Y. Yang, N. Ren, X. Duan, Single-atom catalysts derived from biomass: low-cost and high-performance persulfate activators for water decontamination, *Curr. Opin. Chem. Eng.* 41 (2023), 100942.
- [3] Y. Zhou, X. Liu, Y. Xiang, P. Wang, J. Zhang, F. Zhang, J. Wei, L. Luo, M. Lei, L. Tang, Modification of biochar derived from sawdust and its application in removal of tetracycline and copper from aqueous solution: Adsorption mechanism and modelling, *Bioresour. Technol.* 245 (2017) 266–273.
- [4] S. Liao, B. Pan, H. Li, D. Zhang, B. Xing, Detecting free radicals in biochars and determining their ability to inhibit the germination and growth of corn, wheat and rice seedlings, *Environ. Sci. Technol.* 48 (2014) 8581–8587.
- [5] J. Yu, L. Tang, Y. Pang, G. Zeng, J. Wang, Y. Deng, Y. Liu, H. Feng, S. Chen, X. Ren, Magnetic nitrogen-doped sludge-derived biochar catalysts for persulfate activation: Internal electron transfer mechanism, *Chem. Eng. J.* 364 (2019) 146–159.
- [6] J. Yu, L. Tang, Y. Pang, G. Zeng, H. Feng, J. Zou, J. Wang, C. Feng, X. Zhu, X. Ouyang, J. Tan, Hierarchical porous biochar from shrimp shell for persulfate activation: A two-electron transfer path and key impact factors, *Appl. Catal. B: Environ.* 260 (2020), 118160.
- [7] G. Yin, X. Song, L. Tao, B. Sarkar, A.K. Sarmah, W. Zhang, Q. Lin, R. Xiao, Q. Liu, H. Wang, Novel Fe-Mn binary oxide-biochar as an adsorbent for removing Cd(II) from aqueous solutions, *Chem. Eng. J.* 389 (2020), 124465.
- [8] T. Zhang, C. Li, J. Ma, H. Tian, Z. Qiang, Surface hydroxyl groups of synthetic  $\alpha$ -FeOOH in promoting OH<sup>·</sup> generation from aqueous ozone: Property and activity relationship, *Appl. Catal. B: Environ.* 82 (2008) 131–137.
- [9] J. Bing, C. Hu, L. Zhang, Enhanced mineralization of pharmaceuticals by surface oxidation over mesoporous  $\gamma$ -Ti-Al<sub>2</sub>O<sub>3</sub> suspension with ozone, *Appl. Catal. B: Environ.* 202 (2017) 118–126.
- [10] H. Cao, J. Wang, J.-H. Kim, Z. Guo, J. Xiao, J. Yang, J. Chang, Y. Shi, Y. Xie, Different roles of Fe atoms and nanoparticles on g-C<sub>3</sub>N<sub>4</sub> in regulating the reductive activation of ozone under visible light, *Appl. Catal. B: Environ.* 296 (2021), 120362.
- [11] Y. Pi, J. Schumacher, M. Jekel, Decomposition of aqueous ozone in the presence of aromatic organic solutes, *Water Res* 39 (2005) 83–88.
- [12] M. Ateia, M. Ceccato, A. Budi, E. Ataman, C. Yoshimura, M.S. Johnson, Ozone-assisted regeneration of magnetic carbon nanotubes for removing organic water pollutants, *Chem. Eng. J.* 335 (2018) 384–391.
- [13] Y. Yu, J. Ji, K. Li, H. Huang, R.P. Shrestha, N.T. Kim Oanh, E. Winijkul, J. Deng, Activated carbon supported MnO nanoparticles for efficient ozone decomposition at room temperature, *Catal. Today* (2019).
- [14] S.-Q. Tian, J.-Y. Qi, Y.-P. Wang, Y.-L. Liu, L. Wang, J. Ma, Heterogeneous catalytic ozonation of atrazine with Mn-loaded and Fe-loaded biochar, *Water Res* 193 (2021), 116860.
- [15] L. Fang, K. Liu, F. Li, W. Zeng, Z. Hong, L. Xu, Q. Shi, Y. Ma, New insights into stoichiometric efficiency and synergistic mechanism of persulfate activation by zero-valent bimetal (Iron/Copper) for organic pollutant degradation, *J. Hazard. Mater.* 403 (2021), 123669.
- [16] K. Liu, F. Li, J. Cui, S. Yang, L. Fang, Simultaneous removal of Cd(II) and As(III) by graphene-like biochar-supported zero-valent iron from irrigation waters under aerobic conditions: Synergistic effects and mechanisms, *J. Hazard. Mater.* 395 (2020), 122623.
- [17] H. Li, J. Guo, L. Yang, Y. Lan, Degradation of methyl orange by sodium persulfate activated with zero-valent zinc, *Sep. Purif. Technol.* 132 (2014) 168–173.
- [18] G. Wen, S.-J. Wang, J. Ma, T.-L. Huang, Z.-Q. Liu, L. Zhao, J.-F. Su, Enhanced ozonation degradation of di-n-butyl phthalate by zero-valent zinc in aqueous solution: Performance and mechanism, *J. Hazard. Mater.* 265 (2014) 69–78.
- [19] J.P. Myers, M.N. Antoniou, B. Blumberg, L. Carroll, T. Colborn, L.G. Everett, M. Hansen, P.J. Landrigan, B.P. Lanphear, R. Mesnage, L.N. Vandenberg, F.S. Vom Saal, W.V. Welshons, C.M. Benbrook, Concerns over use of glyphosate-based herbicides and risks associated with exposures: a consensus statement, *Environ. Health* 15 (2016) 19.
- [20] C. Chávez-Moreno, L. Ferrer, L. Hinojosa-Reyes, A. Hernández-Ramírez, V. Cerdá, J. Guzmán-Mar, On-line monitoring of the photocatalytic degradation of 2,4-D and dicamba using a solid-phase extraction-multisyringe flow injection system, *J. Environ. Manag.* 129 (2013) 377–383.
- [21] M.A. Crespin, M. Gallego, M. Valcárcel, J.L. González, Study of the Degradation of the Herbicides 2,4-D and MCPA at Different Depths in Contaminated Agricultural Soil, *Environ. Sci. Technol.* 35 (2001) 4265–4270.
- [22] O. Gimeno, A. Aguinaco, A. Rey, F.J. Beltrán Novillo, J.R. Toledo, Ozonation of 4-chloro-2-methylphenoxyacetic acid (MCPA) in an activated sludge system, *J. Chem. Technol. Biotechnol.* 89 (2014) 1219–1227.
- [23] D. Loomis, K. Guyton, Y. Grosse, F. El Ghissassi, V. Bouvard, L. Benbrahim-Tallaa, N. Guha, H. Mattock, K. Straif, Carcinogenicity of lindane, DDT, and 2,4-dichlorophenoxyacetic acid, *Lancet Oncol.* 16 (2015) 891–892.
- [24] H. Bader, J. Hoigné, Determination of ozone in water by the indigo method, *Water Res* 15 (1981) 449–456.
- [25] D. Ding, L. Zhou, F. Kang, S. Yang, R. Chen, T. Cai, X. Duan, S. Wang, Synergistic adsorption and oxidation of ciprofloxacin by biochar derived from metal-enriched phytoremediation plants: Experimental and computational insights, *ACS Appl. Mater. Interfaces* 12 (2020) 53788–53798.
- [26] T. Lu, F. Chen, Multivfn: A multifunctional wavefunction analyzer, *J. Comput. Chem.* 33 (2012) 580–592.
- [27] M. Frisch, G. Trucks, H. Schlegel, G. Scuseria, M. Robb, J. Cheeseman, G. Scalmani, V. Barone, G. Petersson, H. Nakatsuji, Anonymous (Gaussian 16, Revision B.01), Gaussian, Inc., Wallingford CT, 2016.
- [28] X. Guan, Q. Li, T. Maimaiti, S. Lan, P. Ouyang, B. Ouyang, X. Wu, S.-T. Yang, Toxicity and photosynthetic inhibition of metal-organic framework MOF-199 to pea seedlings, *J. Hazard. Mater.* 409 (2021), 124521.
- [29] J. Wang, S. Wang, Preparation, modification and environmental application of biochar: A review, *J. Clean. Prod.* 227 (2019) 1002–1022.
- [30] B. Lei, J.-I. Fan, A Gradient Weighted Thresholding Method for Image Segmentation, in: X. He, X. Gao, Y. Zhang, Z.-H. Zhou, Z.-Y. Liu, B. Fu, F. Hu, Z. Zhang (Eds.), *Intelligence Science and Big Data Engineering. Image and Video Data Engineering*, Springer International Publishing, Cham, 2015, pp. 300–309.

[31] S. Dong, A. Niu, K. Wang, P. Hu, H. Guo, S. Sun, Y. Luo, Q. Liu, X. Sun, T. Li, Modulation of oxygen vacancy and zero-valent zinc in ZnCr<sub>2</sub>O<sub>4</sub> nanofibers by enriching zinc for efficient nitrate reduction, *Appl. Catal. B: Environ.* 333 (2023), 122772.

[32] I. Hussain, M. Li, Y. Zhang, Y. Li, S. Huang, X. Du, G. Liu, W. Hayat, N. Anwar, Insights into the mechanism of persulfate activation with nZVI/BC nanocomposite for the degradation of nonylphenol, *Chem. Eng. J.* 311 (2017) 163–172.

[33] X. Zhu, J. Shen, J. Kang, P. Yan, L. Yuan, Y. Cheng, B. Wang, S. Zhao, Z. Chen, Surface atomic oxygen species mediated the in-situ formation of hydroxyl radicals on Fe<sub>3</sub>C decorated biochar for enhancing catalytic ozonation, *Chem. Eng. J.* 473 (2023), 145380.

[34] J. Li, D. Yang, X. Zhu, Effects of aging time and annealing temperature on structural and optical properties of sol-gel ZnO thin films, *AIP Adv.* 7 (2017).

[35] I.-H. Yoon, K.-W. Kim, S. Bang, M.G. Kim, Reduction and adsorption mechanisms of selenite by zero-valent iron and related iron corrosion, *Appl. Catal. B: Environ.* 104 (2011) 185–192.

[36] C.H. Choi, S.H. Park, S.I. Woo, Binary and ternary doping of nitrogen, boron, and phosphorus into carbon for enhancing electrochemical oxygen reduction activity, *ACS Nano* 6 (2012) 7084–7091.

[37] F. Banhart, J. Kotakoski, A.V. Krasheninnikov, Structural defects in graphene, *ACS Nano* 5 (2011) 26–41.

[38] S. Zhu, X. Huang, F. Ma, L. Wang, X. Duan, S. Wang, Catalytic removal of aqueous contaminants on N-doped graphitic biochars: Inherent roles of adsorption and nonradical mechanisms, *Environ. Sci. Technol.* 52 (2018) 8649–8658.

[39] H.P. Boehm, Chemical identification of surface groups, *Adv. Catal.* 16 (1966) 179–274.

[40] G. Cai, Z.-I Ye, Concentration-dependent adsorption behaviors and mechanisms for ammonium and phosphate removal by optimized Mg-impregnated biochar, *J. Clean. Prod.* 349 (2022), 131453.

[41] J. He, Y. Long, Y. Wang, C. Wei, J. Zhan, Aerosol-assisted self-assembly of reticulated N-doped carbonaceous submicron spheres for effective removal of hexavalent chromium, *ACS Appl. Mater. Interfaces* 8 (2016) 16699–16707.

[42] K.A. Sharp, B. Honig, Electrostatic Interactions in Macromolecules: Theory and Applications, *Annu. Rev. Biophys. Biophys. Chem.* 19 (1990) 301–332.

[43] Y. Cheng, B. Wang, J. Shen, P. Yan, J. Kang, W. Wang, L. Bi, X. Zhu, Y. Li, S. Wang, L. Shen, Z. Chen, Preparation of novel N-doped biochar and its high adsorption capacity for atrazine based on  $\pi$ - $\pi$  electron donor-acceptor interaction, *J. Hazard. Mater.* 432 (2022), 128757.

[44] Z. Song, Y. Zhang, X. Zhang, X. Zhou, Y. Chen, X. Duan, N. Ren, Kinetics study of chloride-activated peracetic acid for purifying bisphenol A: Role of Cl<sub>2</sub>/HClO and carbon-centered radicals, *Water Res* 242 (2023), 120274.

[45] M. Sui, L. Sheng, K. Lu, F. Tian, FeOOH catalytic ozonation of oxalic acid and the effect of phosphate binding on its catalytic activity, *Appl. Catal. B: Environ.* 96 (2010) 94–100.

[46] Y. Cheng, J. Yang, J. Shen, P. Yan, S. Liu, J. Kang, L. Bi, B. Wang, S. Zhao, Z. Chen, Preparation of P-doped biochar and its high-efficient removal of sulfamethoxazole from water: Adsorption mechanism, fixed-bed column and DFT study, *Chem. Eng. J.* 468 (2023), 143748.

[47] Y. Cheng, Z. Chen, S. Wang, X. Duan, Single atom catalysts for heterogeneous catalytic ozonation, *Curr. Opin. Chem. Eng.* 41 (2023), 100945.

[48] Y. Wang, J. Xi, X. Duan, W. Lv, H. Cao, C. Chen, Z. Guo, Y. Xie, S. Wang, The duet of surface and radical-based carbocatalysis for oxidative destructions of aqueous contaminants over built-in nanotubes of graphite, *J. Hazard. Mater.* 384 (2020), 121486.

[49] Y. Guo, Y. Zhang, G. Yu, Y. Wang, Revisiting the role of reactive oxygen species for pollutant abatement during catalytic ozonation: The probe approach versus the scavenger approach, *Appl. Catal. B: Environ.* 280 (2021), 119418.

[50] Y. Wang, L. Chen, H. Cao, Z. Chi, C. Chen, X. Duan, Y. Xie, F. Qi, W. Song, J. Liu, S. Wang, Role of oxygen vacancies and Mn sites in hierarchical Mn<sub>2</sub>O<sub>3</sub>/LaMnO<sub>3</sub>- $\delta$  perovskite composites for aqueous organic pollutants decontamination, *Appl. Catal. B: Environ.* 245 (2019) 546–554.

[51] W. Li, G.V. Gibbs, S.T. Oyama, Mechanism of ozone decomposition on a manganese oxide catalyst. 1. In situ Raman spectroscopy and ab initio molecular orbital calculations, *J. Am. Chem. Soc.* 120 (1998) 9041–9046.

[52] Z. Song, Y. Zhang, C. Liu, B. Xu, F. Qi, D. Yuan, S. Pu, Insight into-OH and O<sub>2</sub><sup>–</sup> formation in heterogeneous catalytic ozonation by delocalized electrons and surface oxygen-containing functional groups in layered-structure nanocarbons, *Chem. Eng. J.* 357 (2019) 655–666.

[53] Y. Cheng, B. Wang, P. Yan, J. Shen, J. Kang, S. Zhao, X. Zhu, L. Shen, S. Wang, Y. Shen, Z. Chen, In-situ formation of surface reactive oxygen species on defective sites over N-doped biochar in catalytic ozonation, *Chem. Eng. J.* 454 (2023), 140232.

[54] Z. Xiong, B. Lai, Y. Yuan, J. Cao, P. Yang, Y. Zhou, Degradation of p-nitrophenol (PNP) in aqueous solution by a micro-size Fe<sup>0</sup>/O<sub>3</sub> process (mFe<sup>0</sup>/O<sub>3</sub>): Optimization, kinetic, performance and mechanism, *Chem. Eng. J.* 302 (2016) 137–145.

[55] J. Dong, W. Xu, S. Liu, Y. Gong, T. Yang, L. Du, Q. Chen, X. Tan, Y. Liu, Lignin-derived biochar to support CoFe<sub>2</sub>O<sub>4</sub>: Effective activation of peracetic acid for sulfamethoxazole degradation, *Chem. Eng. J.* 430 (2022), 132868.

[56] S. Zhang, D. Wang, X. Quan, L. Zhou, X. Zhang, Multi-walled carbon nanotubes immobilized on zero-valent iron plates (Fe0-CNTs) for catalytic ozonation of methylene blue as model compound in a bubbling reactor, *Sep. Purif. Technol.* 116 (2013) 351–359.

[57] C. Cheng, W. Ren, F. Miao, X. Chen, X. Chen, H. Zhang, Generation of Fe(IV) = O and its Contribution to Fenton-Like Reactions on a Single-Atom Iron-N-C Catalyst, *Angew. Chem., Int. Ed.* 62 (2023), e202218510.

[58] X. Yuan, W. Qin, X. Lei, L. Sun, Q. Li, D. Li, H. Xu, D. Xia, Efficient enhancement of ozonation performance via ZVZ immobilized g-C<sub>3</sub>N<sub>4</sub> towards superior oxidation of micropollutants, *Chemosphere* 205 (2018) 369–379.

[59] Y. Cheng, J. Kang, P. Yan, J. Shen, Z. Chen, X. Zhu, Q. Tan, L. Shen, S. Wang, S. Wang, Surface oxygen vacancies prompted the formation of hydrated hydroxyl groups on ZnO in enhancing interfacial catalytic ozonation, *Appl. Catal. B: Environ.* 341 (2023), 123325.

[60] R. Kumar, P. Gahlyan, N. Yadav, M. Bhandari, R. Kakkar, M. Dalela, A.K. Prasad, Bis-triazolylated-1,4-dihydropyridine - Highly selective hydrophilic fluorescent probe for detection of Fe<sup>3+</sup>, *Dyes Pigments* 147 (2017) 420–428.

[61] J. Chen, R. Qu, X. Pan, Z. Wang, Oxidative degradation of triclosan by potassium permanganate: Kinetics, degradation products, reaction mechanism, and toxicity evaluation, *Water Res* 103 (2016) 215–223.

[62] X. Ren, Y. Sun, L. Zhu, Z. Cui, Theoretical studies on the OH-initiated photodegradation mechanism of dicofol, *Comput. Theor. Chem.* 963 (2011) 365–370.

[63] A. Topalov, B. Abramović, D. Molnár-Gábor, J. Csanádi, O. Arcson, Photocatalytic oxidation of the herbicide (4-chloro-2-methylphenoxy)acetic acid (MCPA) over TiO<sub>2</sub>, *J. Photochem. Photobiol. A: Chem.* 140 (2001) 249–253.

[64] J. Cai, M. Zhou, W. Yang, Y. Pan, X. Lu, K.G. Serrano, Degradation and mechanism of 2,4-dichlorophenoxyacetic acid (2,4-D) by thermally activated persulfate oxidation, *Chemosphere* 212 (2018) 784–793.